

# Tailoring non-collinear magnetism and $3d - 4f$ exchange interactions in $\text{RVO}_3$ epitaxial thin films

Olivier Copie,<sup>1,\*</sup> Julien Varignon,<sup>2</sup> Ingrid Cañero Infante,<sup>3</sup> Mariam Martirosyan,<sup>1</sup> Fadi Choueikani,<sup>4</sup> Philippe Ohresser,<sup>4</sup> Pierre-Eymeric Janolin,<sup>5</sup> Alain Pautrat,<sup>2</sup> Adrian David,<sup>2</sup> Philippe Ghosez,<sup>6</sup> and Wilfrid Prellier<sup>2</sup>

<sup>1</sup>*Université de Lorraine, CNRS, IJL, F-54000 Nancy, France*

<sup>2</sup>*CRISMAT, CNRS, Normandie Université, ENSICAEN, UNICAEN, F-14000 Caen, France*

<sup>3</sup>*Institut des Nanotechnologies de Lyon, CNRS ECL INSA UCBL CPE, F-69621 Villeurbanne, France*

<sup>4</sup>*Synchrotron SOLEIL, L'Orme des Merisiers, F-91190 Saint-Aubin, France*

<sup>5</sup>*Université Paris-Saclay, CentraleSupélec, CNRS, Laboratoire SPMS, 91190, Gif-sur-Yvette, France*

<sup>6</sup>*Theoretical Materials Physics, Q-MAT, Université de Liège, B-4000 Liège, Belgium*

## Abstract

In orthorhombic perovskite oxides ( $\text{RMO}_3$ ), substituting  $\text{R}^{3+}$  rare-earth cations tailors the spin, orbital, and charge degrees of freedom of the central  $\text{M}^{3+}$  transition metal cations through lattice distortions. In turn, these modify also the surrounding environment of  $\text{R}^{3+}$ . When both  $\text{R}^{3+}$  and  $\text{M}^{3+}$  exhibit magnetic properties, phenomena such as spin reorientation and magnetization reversal can occur. In fact, the underlying exchange interactions between  $\text{M}$ - $3d$  spins and  $\text{R}$ - $4f$  magnetic moments enrich the multifunctional character of  $\text{RMO}_3$ , particularly when combined with structural distortions. They play a crucial role in achieving appealing properties such as robust magnetoelectricity with non-collinear magnetic orders. Here, we explore the exchange coupling in epitaxial  $\text{PrVO}_3$  thin films, selectively probing the magnetism of cation sublattices, and uncovering simultaneous  $\text{V}^{3+}$   $3d$  spin reorientation and  $\text{Pr}^{3+}$   $4f$  magnetization reversal using spectroscopy techniques. By strain engineering, we manipulate the lattice distortions to rationalize their role in coupling  $3d$  spins and  $4f$  magnetic moments. Theoretical calculations show that octahedral rotations and Jahn-Teller distortions act as tuning mechanisms, promoting competition between orbital and spin orders. The observed coupling between magnetic cations and lattice distortions can be extended to other orthorhombic  $\text{RMO}_3$  systems, advancing the understanding of controlling spins in engineered perovskite heterostructures and superlattices.

---

\* olivier.copie@univ-lorraine.fr

## I. INTRODUCTION

Understanding the complexity of transition metal oxides (TMO) requires the consideration of the many degrees of freedom exhibited by the electrons in the solid. Additionally, the lattice structure can influence significantly the physical properties, and even a slight change in the crystal structure results in notable changes in the functional properties [1]. Over decades, extensive research has been dedicated to comprehending the intricate interplay among spin, orbital and charge orders in the perovskite oxide compounds [2, 3]. These concurrently active degrees of freedom give rise to a multitude of correlated electronic states that underlie the richness of the functionalities [4]. This diversity fuels a strong interest in delving into the fundamentals and the potential applications of perovskite-related materials [5]. Due to the perovskite structure's inherent ability to distort,  $\text{RMO}_3$  can accommodate many atoms of the periodic table, with different atomic radii. When both  $\text{R}^{3+}$  and  $\text{M}^{3+}$  ions are magnetic, intriguing magnetic behavior are reported [6], such as the change of the spin direction along different crystallographic axes or the inversion of the net magnetization of the crystal. These phenomena, known as spin reorientation and magnetization reversal, hold significant importance for applications [7]. Additionally, complex non-collinear magnetic orders may manifest, breaking inversion symmetries and inducing an electric polarization [6, 8], resulting in a robust magnetoelectric response [9]. This interplay of magnetic and electric properties further intensifies the interest in these materials [10].

Here, we study the magnetic coupling in epitaxial  $\text{RVO}_3$  thin films between  $\text{R}^{3+}$  ( $\text{R} = \text{Pr}$ ) and  $\text{V}^{3+}$ . We selectively probed the magnetic behavior of the cation sublattices and observed the simultaneous  $\text{V}^{3+}$   $3d$  spin reorientation and  $\text{Pr}^{3+}$   $4f$  magnetic moments reversal, both dependent on the temperature and magnetic field. Through strain engineering, we precisely tailored the lattice structure, which in turn modifies the lattice distortion such as the oxygen octahedra rotation, involved in the couplings between  $3d$  and  $4f$  magnetic moments [11]. This exchange striction interaction, beside the understanding of the robust magnetoelectricity in orthorhombic perovskite [12], is important for designing artificial multiferroic superlattices [13–15].

To accommodate the mismatch between  $\text{R}-\text{O}$  and  $\text{M}-\text{O}$  bond lengths,  $\text{RMO}_3$  commonly adopts a  $Pbnm$  orthorhombic structure, characterized by cooperative oxygen octahedron rotations, as illustrated in Figure 1(a) featuring the tilted  $\text{MO}_6$  octahedra (in blue) with the

central  $M^{3+}$  ion. The rotations also modify the local environment around the  $R^{3+}$  cation, which is surrounded by 12 oxygen atoms forming a cuboctahedron, as depicted in Figure 1(a) (in green). Additionally, due to the change of the R–O covalency, the rotations of the  $MO_6$  octahedra lead to a shift of  $R^{3+}$  ions from their position in cubic symmetry [16], being a key parameter of hybrid improper ferroelectricity [17, 18]. All these atomic displacements resulting from structural changes alter the orbital occupancy and electron transfer between neighboring atoms, potentially giving rise to complex orbital and spin ordered phases in  $RVO_3$  compounds and others [19–22].

While the  $3d$  delocalized electrons are sensitive to the strength of the crystal field, the  $4f$  localized electrons undergo a large spin-orbit coupling (SOC) that enhances the magnetic anisotropy. Therefore, beyond merely considering the  $M^{3+}$  ion and the structural distortion of its closest neighborhood, the role of the magnetic exchange between the  $M^{3+}$  and  $R^{3+}$  sublattices should be investigated [11, 23]. We point out that, recently, the effects of rare earth magnetism and  $4f$  electrons have also been the focus of attention with regard to the superconducting properties of the infinite-layer  $RNiO_2$  system [24, 25].

$RVO_3$  compounds have emerged as an intriguing material, drawing significant interest to better understand the properties of TMO. Noteworthy features include a complex yet prototypical interplay between spin, orbital, and charge orders, coupled with crystalline lattice distortions, such as relatively weak Jahn-Teller (JT) distortions [19]. In contrast to  $Mn^{3+} e_g$  electrons in  $RMnO_3$ , the JT distortions of the two  $t_{2g}$  electrons at  $V^{3+}$  sites subtly bias the orbital ordering [26]. The cooperative  $VO_6$  rotations are described by an  $a^-a^-c^+$  tilt pattern according to Glazer’s notation [27] (out-of-phase rotation  $\varphi_x^-$  ( $\varphi_y^-$ ) along the  $[100]_c$  ( $[010]_c$ ) axis, and in-phase rotation  $\varphi_z^+$  along the  $[001]_c$  axis, c for cubic) [21]. This JT distortion, consisting in long and short V–O bonds length along the  $[100]_c$  and  $[010]_c$  pseudo-cubic directions [28], allows lifting the degeneracy between the V  $t_{2g}$  levels. The two electrons per  $V^{3+}$  sites are then ideally located either in the  $d_{xz}$  or in the  $d_{yz}$  orbitals,  $d_{xy}$  being always occupied. As the temperature decreases,  $RVO_3$  undergo a structural phase transition from orthorhombic  $Pbnm$  to monoclinic  $P2_1/b$  [19, 21]. Concurrently, the cooperative JT distortions promote a G-type orbital order ( $G_{OO}$ ) of V  $t_{2g}$  orbitals, as presented in Figure 1(b), at the temperature  $T_{OO}$ . At lower temperature, superexchange interactions then stabilize a C-type antiferromagnetic spin order ( $C_{SO}$ ) of the  $V^{3+}$  spins at the temperature  $T_{SO}$ , as shown in Figure 1(b), also referred as Néel temperature. As  $R^{3+}$  ionic size decreases, the

$\text{VO}_6$  rotations increase and  $T_{\text{SO}}$  decreases monotonously with the V  $3d - \text{O } 2p$  orbitals overlap reduction, as for  $\text{RCrO}_3$  or  $\text{RFeO}_3$  [29]. For small  $\text{R}^{3+}$  ionic radii, a structural transition back to  $Pbnm$  occurs, accompanied by a spin/orbital reorderings from  $\text{C}_{\text{SO}}/\text{G}_{\text{OO}}$  to  $\text{G}_{\text{SO}}/\text{C}_{\text{OO}}$  [19].

## II. EXPERIMENTAL AND THEORETICAL METHODS

40 nm-thick  $\text{PrVO}_3$  thin films were deposited onto  $(001)_c$ -oriented  $\text{SrTiO}_3$  substrates by PLD, firing on a polycrystalline  $\text{PrVO}_4$  target. The latter was prepared via standard solid-state reaction from a stoichiometric  $\text{Pr}_6\text{O}_{11}$  and  $\text{V}_2\text{O}_5$  powders, subsequently pressed into pellets and sintered in air at  $1100^\circ\text{C}$  for 48 hours. The KrF excimer laser ( $\lambda = 248 \text{ nm}$ ) was focused on the target with a repetition rate and a fluence set at 2 Hz and  $2 \text{ J.cm}^{-2}$ , respectively. Prior to deposition, the substrates underwent cleaning in acetone and propanol. The deposition was carried out within a growth temperature range of  $500^\circ\text{C}$  to  $800^\circ\text{C}$ , maintaining the growth pressure fixed to  $8 \times 10^{-6} \text{ mbar}$ . The lattice parameters were determined using X-ray diffraction with a Malvern PANalytical X'pert Pro MRD diffractometer, with a monochromatic Cu  $K\alpha_1$  radiation ( $\lambda = 1.54056 \text{ \AA}$ ).

The macroscopic magnetization was measured in DC mode using a superconducting quantum interference device (SQUID) magnetometer. A magnetic field  $\mathbf{B}$  was applied parallel and perpendicular to the film surface, employing a Quantum Design MPMS ( $\pm 50 \text{ kOe}$ ) and MPMS3 ( $\pm 70 \text{ kOe}$ ), respectively. The measured magnetization was corrected by subtracting the substrate diamagnetic contribution. The FC (Field Cooled) –ZFC (Zero Field Cooled) protocol consisted in cooling down the sample with  $|\mathbf{B}| = 5 \text{ kOe}$ , then measuring the magnetization as function of the temperature up to 300 K with  $|\mathbf{B}| = 50 \text{ Oe}$ , and cooling down the sample without applied magnetic field, then measuring the magnetization as function of the temperature up to 300 K with  $|\mathbf{B}| = 50 \text{ Oe}$ .

Soft X-ray absorption spectroscopy (XAS) and X-ray magnetic circular dichroism (XMCD) were performed at the DEIMOS beamline of the French Synchrotron Facility SOLEIL [30]. XAS is a powerful technique due to its chemical/orbital selectivity and sensitivity to the crystalline environment of the absorber atom. XMCD provides information such as the spin and orbital magnetic moments without the substrate's contribution. Consequently, we selectively probed the roles of the  $\text{V}^{3+}$  and the  $\text{Pr}^{3+}$  magnetic sublattices. The V- $L_{2,3}$  edges

correspond to the excitation of photoelectrons from the spin-orbit split  $2p_{1/2}$  and  $2p_{3/2}$  levels to spin-split  $3d$  level and the Pr- $M_{4,5}$  edges correspond to the  $3d_{3/2}$  and  $3p_{5/2}$  to  $4f$  transitions. Additionally, spectra at the O-K edge were recorded, corresponding to the excitation of photoelectrons from the O  $1s$  orbital to O  $2p$  orbitals, which are hybridized with the empty orbital states of the V and Pr cations. The measurements were carried out using the total electron yield (TEY) mode. The temperature ranged from 5 K to 300 K, with the applied magnetic field of  $\pm 65$  kOe directed along the X-ray beam. Eight absorption spectra were acquired across the V- $L_{2,3}$  and O-K (from 510 to 550 eV) and Pr- $M_{4,5}$  (from 920 to 970 eV) edges, alternating opposite magnetic field directions and left/right circular (CL/CR) light polarization, and then averaged to obtain the  $\mu_{\text{CR}}$  and  $\mu_{\text{CL}}$  spectra. Subsequently, the XMCD spectra were calculated as the difference  $0.5 \times (\mu_{\text{CR}} - \mu_{\text{CL}})$ . The probing depth is approximately 6 nm and 15 nm around 550 eV and 950 eV, respectively. The first XAS and XMCD spectra from 0 to 65 kOe were measured after zero field cooling. The magnetic field-dependent XMCD loops at the V- $L_3$  and Pr- $M_4$  edges peaks were obtained by measuring, at each field, the difference between the intensity for CR and CL light polarization, normalized by the intensity before the absorption edge. The energy resolution of the XAS and XMCD experiments were around 0.06 eV and 0.15 eV across the V- $L_{2,3}$ /O-K and the Pr- $M_{4,5}$ , respectively. From the XMCD spectra, quantitative information such as the orbital ( $\langle L_z \rangle$ ) and the spin ( $2\langle S_z \rangle$ ) moments can be extracted using the so-called sum-rules [31, 32]. Unfortunately, the large overlap between the V- $L_2$  and  $L_3$  edges complicates the application of the rules for the determination of  $\langle S_z \rangle$ . As detailed later in the text, the spin sum rule is also invalid for light rare earths such as Pr. Therefore, we have only applied the orbital sum rule Pr- $M_{4,5}$  edges. Hence,  $\langle L_z \rangle = (4l + 2 - n) \times q/r$  with  $q = \int_{M_4+M_5} (\mu_{\text{CR}} - \mu_{\text{CL}}) dE$  and  $r = \int_{M_4+M_5} 0.5 \times (\mu_{\text{CR}} + \mu_{\text{CL}}) dE$ . The transitions into the higher unoccupied states or into the continuum have been corrected in the XAS spectra by a two step-like function. In the case of Pr<sup>3+</sup> ( $4f^2$ ), the angular moment  $l$  is 3, and the occupation number  $n$  is 2, *i.e.* the number of holes is 12.

The density functional theory (DFT) calculations were carried out using the VASP package [33, 34]. A  $4 \times 4 \times 4$   $k$ -point grid was utilized for the 40 atoms  $Pbnm$  ( $P2_1/b$ ) phases and their respective symmetry lowered  $P2_1/m$  ( $P\bar{1}$ ) film structures. The energy cutoff was set to 500 eV. The convergence of the self-consistent field was achieved until the energy difference between consecutive steps was lower than  $10^{-9}$  eV. The geometry relaxations were

conducted until forces were lower than 0.1 meV/Å. We used the Projector Augmented-Wave method (PAW) with the following valence electrons:  $5s^25p^66s^0$  for  $\text{Pr}^{3+}$ , the two extra  $4f^2$  electrons are either frozen in the pseudopotential or treated explicitly ;  $3s^23p^64s^03d^2$  for  $\text{V}^{3+}$  ;  $2s^22p^6$  for  $\text{O}^{2-}$ . By default, the Pr  $4f$  electrons are frozen in the pseudopotential, while their explicit treatment is only considered when addressing the magnetism at Pr site. We employed the PBE functional revised for solids (PBEsol) [35]. To account for the strong correlation of the  $\text{V}^{3+} - t_{2g}$  electrons [36], the effective U parameter acting on V  $d$  orbitals is fixed to  $U_{\text{eff}} = 3.5$  eV, a value previously shown to reproduce the  $\text{RVO}_3$  phase diagram [14] as well as the experimental trend of the Néel temperature of  $\text{PrVO}_3$  experiencing epitaxial and/or chemical strain [38, 39]. Unless stated, DFT calculations are performed without Pr  $4f$  electrons. For calculations involving Pr  $4f$  electrons, delocalization errors inherent to the implementation of DFT being larger for  $4f$  orbitals than for  $3d$  orbitals, we opted for an effective parameter  $U_{4f}$  of 5 eV acting on Pr  $4f$  states. This value appears as a fair choice reproducing a more stable V- $C_xC_z$  Pr- $C_xC_z$  magnetic solution than a V- $G_y$  Pr- $C_xC_z$  in the bulk  $\text{PrVO}_3$  [ $\Delta E = -5.65$  meV (f.u) $^{-1}$ ], in agreement with experimental observations (see Supplemental Material [40]). The spins were treated at the collinear and non-collinear levels, and two different antiferromagnetic spin orderings were used, namely  $C_{\text{SO}}$  and  $G_{\text{SO}}$  spin orders for V. The insulating  $C_{\text{SO}}/G_{\text{OO}}$  ground state of the bulk  $\text{PrVO}_3$  is correctly predicted by preliminary DFT calculations. In the case of  $\text{PrVO}_3$  on  $(001)_c$ -oriented  $\text{SrTiO}_3$ , the  $[001]$  and  $[\bar{1}\bar{1}0]$  orthorhombic axes were aligned along the in-plane cubic axes of substrate while the  $[110]$  axis was forced to be orthogonal.  $\text{PrVO}_3$  then adopts a  $P2_1/m$  symmetry with a  $C_{\text{OO}}/G_{\text{SO}}$  ground state. The strain was treated as an uniaxial constraint on the  $[110]$  direction of the film and only atomic positions were relaxed.

### III. RESULTS AND DISCUSSION

We have deposited  $\text{PrVO}_3$  epitaxial films by pulsed laser deposition (PLD) on  $(001)_c$ -oriented  $\text{SrTiO}_3$  cubic substrate (see above). The orthorhombic  $Pbnm$  symmetry is lowered to the monoclinic  $P2_1/m$  one, the long  $c$ -axis being clamped by one of the in-plane substrate cubic directions, as the in-phase octahedral rotation of  $\text{PrVO}_3$  [37, 38]. The uniaxial strain along the  $[110]$  direction was then tailored by controlling the oxygen exchange between the substrate and the film during the growth [39], increasing the unit cell volume  $V_{\text{UC}}$ . We point

out that the (110)-oriented films maintain some structural degrees of freedom that enable them to undergo the symmetry change compatible with the spin orderings. The structural characterizations of the heterostructures, including measurements at low temperatures, are given in the Supplemental Material [40].

### A. Spin reorientation.

In Figure 1(c)–(f), we depict the magnetization as a function of an applied in-plane magnetic field  $\mathbf{B}$  after zero field cooling. At 10 K, a hysteretic behavior with a coercive field ( $H_C$ ) of approximately 30 kOe is observed. At remanence, the net magnetization should result from the canting of the  $V^{3+}$  spins due to the antisymmetric exchange interaction  $\mathbf{D}_{ij} \cdot (\mathbf{S}_i \times \mathbf{S}_j)$ , where  $\mathbf{D}_{ij}$  is the Dzyaloshinskii-Moriya term and  $\mathbf{S}_{i(j)}$  the spin moment at site  $i(j)$ . In Figure 1(c), the net magnetization linearly increases with  $\mathbf{B}$  from 10 kOe up to the saturation, typical of  $\mathbf{B}$  perpendicular to the easy axis of the antiferromagnetically coupled sublattices (small  $V_{UC}$ ). Below 10 kOe, a zero net magnetization plateau is observed, widening with increasing  $V_{UC}$ . In Figure 1(f), the plateau extends to 30 kOe. Above, the magnetization rises rapidly until saturation, representing  $\mathbf{B}$  being parallel to the easy axis before a metamagnetic transition clearly seen for larger  $V_{UC}$ . The magnetic hysteresis evolution [Figure 1(c)–(f)] suggests a competition or coexistence of the two spin orientations with varying  $V_{UC}$ . In the bottom panel of Figure 1(k), the saturation magnetization ( $M_S$ ) and remanence ( $M_R$ ) increases as  $V_{UC}$  decreases. This implies an energetically more favorable orientation of  $\mathbf{B}$  relative to the spins' easy axis, specifically perpendicular in the case of antiferromagnets with high anisotropy energy compared to the exchange energy of the magnetic sublattices. Consequently, modifying the  $\text{PrVO}_3$  unit cell strain provides a control of the anisotropy energy and may influence different spin orientations.

### B. Magnetization reversal.

In Figure 1(g)–(j), we present the temperature-dependence of the magnetization following the FC – ZFC protocol (see above). For the FC curve, the magnetic signal increases as the temperature decreases, corresponding to the ordering of the  $V^{3+}$  spins at  $T_{SO}$ . For the ZFC, it turns negative below  $T_{SO}$  down to 10 K as seen in the insets. In details, the



magnetization initially increases at  $T_{\text{SO}}$ , then it reverses, crosses zero few degrees below and becomes more negative as  $V_{\text{UC}}$  increases. This behavior is archetypal of the existence of two distinct magnetic sublattices with equal magnetic moments compensating each other at the so-called compensation temperature ( $T_{\text{COMP}}$ ) until the magnetic moment of a sublattice prevails at lower temperature. In Figure 1(k), we display  $T_{\text{SO}}$  and  $T_{\text{COMP}}$  as a function  $V_{\text{UC}}$ . The non-monotonous evolution of  $T_{\text{SO}}$  has been elucidated by considering the opposing behavior of intra-plane and inter-plane magnetic superexchange interactions between nearest neighbors  $V^{3+}$  sites [39]. Although  $T_{\text{COMP}}$  behaves similarly, the difference with  $T_{\text{SO}}$  increases monotonously with  $V_{\text{UC}}$ , suggesting a structural bias between magnetic sublattices at different crystallographic sites. In  $\text{RVO}_3$ , the temperature-induced magnetization reversal has been attributed to simultaneous switching of the spin and orbital orders in  $\text{YVO}_3$  [51] or spin imbalance between two inequivalent  $V^{3+}$  sublattices in  $\text{SmVO}_3$  and  $\text{NdVO}_3$  [52, 53]. Furthermore, the magnetic moment carried by  $R^{3+}$  can influence the magnetic phase diagram of  $\text{RVO}_3$  as observed in bulk by neutron diffraction [54–56]. We see a distinct jump at zero magnetic field in the magnetic hysteresis loops depicted in Figure 1. This is attributed to the paramagnetic contribution of isolated  $\text{Pr}^{3+}$  cations owing to the overoxidation of the film surface after air exposure and the presence of  $V^{4+}$  cations [46]. This effect is commonly observed at the surface of TMO [57, 58]. But intuitively, this points the existence of a magnetic coupling between  $\text{Pr}^{3+}$  and  $V^{3+}$  in stoichiometric  $\text{PrVO}_3$ .

### C. Ferrimagnetic coupling.

To investigate the magnetic and structural couplings in the  $\text{PrVO}_3$  thin films, we have selectively probed the magnetic properties of the  $V^{3+}$  and  $\text{Pr}^{3+}$  sublattices by using XAS and XMCD (if not specified, the measurements are performed on the film #4). The experimental geometry is illustrated in Figure 2(a) and shows the parallel alignment of the incoming polarized light, the magnetic field  $\mathbf{B}$  and the [110] direction, being the quantization axis. In Figure 2(b) and (c), the XAS spectra measured at 5 K, with  $|\mathbf{B}| = 65$  kOe, are presented for the  $V\text{-L}_{2,3}$  and  $\text{Pr}\text{-M}_{4,5}$  edges, respectively. In comparison with spectra of the literature, the  $V\text{-L}_{2,3}$  spectral line shape reveals a mixture of  $V^{3+}$  (around 516 eV) and  $V^{4+}$  around (around 517.5 eV) [45] at the very surface (see Figure S3 and Figure S4 in ref. [40]), while the  $\text{Pr}\text{-M}_{4,5}$  edges fine structures are characteristic of  $\text{Pr}^{3+}$  ions only and in very good

agreement with atomic calculations considering a quantum number  $j = 4$  ground state [47]. Figure 2(b) and (c) display also the corresponding XMCD spectra. A small dichroic signal at the V-L<sub>2,3</sub> edges indicates a net magnetic moment, along the [110] direction, due to the canted V spins. We observe also a large dichroic signal at the Pr-M<sub>4,5</sub>. According to our experimental geometry the Pr and V total magnetic moments, projected along the [110] direction, are parallel. Figure 2(d) and (e) depict the magnetic field dependence of the XMCD signal at the V-L<sub>3</sub><sup>(1)</sup> edge (516 eV) and the M<sub>4</sub> (954 eV) edges. The similar shape and width of the hysteresis loops indicate the mutual follow-up and rotation of the Pr and V moments during the field switching. Within experimental accuracy, the deduced coercive fields are fairly similar:  $8.7 \pm 1$  kOe (V-L<sub>3</sub>) and  $6.3 \pm 0.5$  kOe (Pr-M<sub>4</sub>), providing a direct evidence of the existence of two coupled magnetic sublattices in PrVO<sub>3</sub>. We point out that the hysteretic behavior is only observed when measured at the V-L<sub>3</sub><sup>(1)</sup> edge, whereas a reversible slope is observed at the V-L<sub>3</sub><sup>(2)</sup> edge and confirms the isolated and paramagnetic character of the V<sup>4+</sup> cations at the very surface in Figure 2(d). In Figure 2(d) and (e), the linear and reversible XMCD loops at the V-L<sub>3</sub><sup>(1)</sup> and Pr-M<sub>4</sub> edges at 125 K demonstrate the paramagnetic behavior above T<sub>SO</sub>, further supporting the intrinsic magnetic coupling of the V<sup>3+</sup> and Pr<sup>3+</sup> sublattices in PrVO<sub>3</sub>. Although, the so-called sum rules are powerful for the quantitative analysis of XMCD spectra [31, 32], care must be taken when using them on early transition metals, especially for the spin momentum  $\langle S_z \rangle$ . For the orbital momentum  $\langle L_z \rangle$ , as it is proportional to the total integrated spectrum, the zero integrated V-L<sub>2,3</sub> dichroic signal indicates the orbital moment is zero (see Figure S5 in ref. [40]). Despite, we consider the shaded area under V-L<sub>1</sub><sup>(2)</sup> in Figure 2(b) as representative of the V<sup>3+</sup> total moment. The area is denoted as  $\mathcal{A}_{V^{3+}}$ . For Pr<sup>3+</sup>, only the orbital sum rule can again be applied. Indeed, strong Coulomb interactions between the 4*f* electrons and the 3*d* core hole lead to a significant deviation of the  $\langle S_z \rangle$  calculated values [59, 60], which prohibits considering it here. Nevertheless, as the Pr<sup>3+</sup> shape is well reproduced by atomic calculations in a  $j = 4$  ground state [47], we assume the orbital moment dominates and  $\langle L_z \rangle$  serves, from here, as a proxy catching the magnetic behavior of the 4*f*<sup>2</sup> electrons in PrVO<sub>3</sub>. Using the orbital sum rule, we determined  $\langle L_z \rangle = -1.11 \mu_B \text{ at.}^{-1}$  for Pr<sup>3+</sup> (see above), at 5 K,  $|\mathbf{B}| = 65$  kOe, and maximum when  $\mathbf{B}$  is along [110] (see Figure S4 in ref. [40]). As Pr<sup>3+</sup> cation has less than half-filled shells,  $\langle L_z \rangle$  and  $\langle S_z \rangle$  combine as  $2\langle S_z \rangle$  reduces the dominating contribution of  $\langle L_z \rangle$  to the total magnetic moment. Consequently, the total magnetization of PrVO<sub>3</sub> is

the result of a balance between  $V^{3+}$  spins and  $Pr^{3+}$  orbital and spin moments.

#### D. 4f polarized moments and 3d ordered spins.

Figure 3(a) and (b) illustrate the XMCD spectra at the V-L<sub>2,3</sub> and Pr-M<sub>4,5</sub> edges, respectively, with  $|\mathbf{B}| = 65$  kOe, across varying the temperature. The  $V^{3+}$  dichroic signal exhibits a rapid initial drop, followed by a smooth decrease upon heating to 300 K. The  $Pr^{3+}$  dichroic signal gradually decreases up to 300 K. In Figure 3(c), we show the integrated dichroic signal  $\mathcal{A}_{V^{3+}}$  and  $\langle L_z \rangle$  against the temperature. Below 100 K,  $\mathcal{A}_{V^{3+}}$  shows a notable increase, and a comparable trend is observed for  $\langle L_z \rangle$  amplitude. This agrees with the onset of the  $V^{3+}$  spin ordering at  $T_{SO} = 81$  K [see Figure 1(j)]. The inset in Figure 3(c) displays the inverse of  $\mathcal{A}_{V^{3+}}$  as a function of the temperature. The inverse of  $\mathcal{A}_{V^{3+}}$  versus temperature conforms to a Curie-Weiss law  $\propto (T + \theta)/C_{V^{3+}}$ , where  $C_{V^{3+}}$  is the Curie constant of the transition metal sublattice, and  $\theta$  is the Weiss temperature being negative and characterizing the resistance to parallel alignment of the  $V^{3+}$  spins. The  $Pr^{3+}$  contribution to the total magnetization is found to rise around  $T_{SO}$ . Moreover, we observe that the dichroism at the Pr-M<sub>4,5</sub> edges persists, as shown in the inset of Figure 3(b), without applied magnetic field up to 40 K. Both temperature-dependence and persistence of the Pr-M<sub>4,5</sub> edges dichroism further agree with an exchange interaction between the ordered  $V^{3+}$  spins and the paramagnetic  $Pr^{3+}$  moments, yielding a polarized  $Pr^{3+}$  sublattice. The calculated momenta yield of  $\langle L_z \rangle$  is  $-0.12 \mu_B \text{ at.}^{-1}$  and  $0.13 \mu_B \text{ at.}^{-1}$  at 5 K and 40 K, respectively. Eventually, this reversal shows that the balance between the magnetic sublattices is temperature dependent and may be canceled out at  $T_{COMP}$  as observed in Figure 1.

#### E. Non-collinear magnetism.

In Figure 4(a) and (b), we present the XMCD spectra recorded at 5 K following ZFC for the V-L<sub>2,3</sub> and Pr-M<sub>4,5</sub> edges, respectively. The dichroic  $V^{3+}$  and  $Pr^{3+}$  signals exhibit an increase with changing  $\mathbf{B}$ . The insets compare the XMCD spectra measured at zero field, after ZFC (light brown) and after saturation (dark brown). While the V-L<sub>2,3</sub> XMCD signal at remanence indicates a net moment carried by  $V^{3+}$ , the one after ZFC corresponds to the derivative of the XAS spectra (not shown), indicating there is no sizable net moment

projected along the [110] direction after ZFC. The Pr-M<sub>4,5</sub> signal is dichroic both after ZFC and at remanence, but with opposite signs at the Pr-M<sub>4</sub> edge and smaller intensity after ZFC. Since the maximum dichroic intensity occurs when the magnetization direction (quantization axis) is aligned with the photon spin direction [61], the smaller intensity after ZFC indicates a resulting magnetic moment either very small or moving away from the [110] direction. In Figure 4(c), we present the  $\mathbf{B}$  dependence of  $\mathcal{A}_{V^{3+}}$ . It displays a metamagnetic-like transition with increasing  $\mathbf{B}$ .  $\mathcal{A}_{V^{3+}}$  increases gradually between 0 and  $\sim 20$  kOe, stabilizes between 20 and 40 kOe, and then increases proportionally to  $\mathbf{B}$ . We propose the following scenario, considering the projection of the magnetic moment along the direction of  $\mathbf{B}$ . (1) after ZFC, the V<sup>3+</sup> spins are antiparallel, resulting in no sizable magnetization, as depicted in Figure 4(c). As  $\mathbf{B}$  is perpendicular to the spin easy axis (red dashed line), the spins of the V<sup>3+</sup> sublattice cant in the direction of  $\mathbf{B}$ , gradually building up a net magnetization between (1) and (2). The plateau between (2) and (3) suggests that the anisotropy energy is not compensated by  $\mathbf{B}$ , which occur between (3) to (4) where the V<sup>3+</sup> spins cant further as  $\mathbf{B}$  increases. This implies the rotation of the spin easy axis, becoming parallel to  $\mathbf{B}$ . As shown in Figure 1(b), the spin axes of G<sub>SO</sub> and C<sub>SO</sub> are perpendicular. We note that first-principles calculations using density functional theory (DFT) have shown that at the collinear level (see above), PrVO<sub>3</sub> adopts a  $P2_1/m$  symmetry with a G<sub>SO</sub> ground state for the V<sup>3+</sup> spins without  $\mathbf{B}$ . Therefore, we rationalize the reorientation of the V<sup>3+</sup> spins with  $\mathbf{B}$  as a spin ordering transition from G<sub>SO</sub> to C<sub>SO</sub>. To tackle the magnetic behavior of the Pr<sup>3+</sup> sublattice in the presence of a magnetic field, we present the field-dependence of  $\langle L_z \rangle$  in Figure 4(c). At  $|\mathbf{B}| = 0$ ,  $\langle L_z \rangle = 0.18\mu_B \text{ at.}^{-1}$  and at 10 kOe, it reverses to  $-0.490\mu_B \text{ at.}^{-1}$ , remaining globally proportional to  $\mathbf{B}$ . At remanence  $\langle L_z \rangle$  remains negative ( $-0.12 \mu_B \text{ at.}^{-1}$ ). It seems that the V<sup>3+</sup> reordering affects the Pr<sup>3+</sup> magnetic moment direction or reciprocally.

To get insights on the potential magnetic structures of the film, we have performed DFT simulations considering the two non-collinear magnetic structures that are proposed for V C<sub>SO</sub> and V G<sub>SO</sub> experimentally – namely C<sub>x</sub>C<sub>z</sub> and G<sub>y</sub> in Bertaut’s notation for a  $Pbnm$  cell of with  $a^- a^- c^+$  octahedral rotations, respectively. We then include the 4f Pr spins forming a C<sub>x</sub>C<sub>z</sub> spin order as proposed in bulk compounds whatever the V spin orders or forced it to be ferromagnetically aligned along  $z$  to mimic the Pr spin reorientation with an external magnetic field observed experimentally. The ground state corresponds to a C-type

AFM ordering of the  $\text{Pr}^{3+}$  magnetic moments associated to G-type  $\text{V}^{3+}$  spin order [40]. The average magnetic moment carried by height sites is close to  $0.1\mu_B$  per 8 f.u. along the [001] and [110] directions, and around  $-0.04\mu_B$  (8 f.u.)<sup>-1</sup> along the  $[\bar{1}\bar{1}0]$  direction for both  $\text{V}^{3+}$  and  $\text{Pr}^{3+}$  (see Table S3 in ref. [40]). A magnetic configuration with a  $\text{Pr}^{3+}$  C-type ordering is also found with  $\text{C}_{\text{SO}}$  ( $\Delta E = +10$  meV), whose net magnetization is rather small (see Table S4 in ref. [40]). In Figure 4(d), we have sketched the average magnetic moments at just one of height sites in the supercell (blue vector for  $\text{V}^{3+}$  at the center of a pseudo-cubic cell and orange vector for  $\text{Pr}^{3+}$  at the corner of a pseudo-cubic cell) for the calculated magnetic configurations. Moreover, we have also calculated the case where the  $\text{Pr}^{3+}$  spins are freezed along the [110] direction (the orbital moment adapts to SOC), mimicking a ferromagnetic alignment (F-type) with  $\mathbf{B}$ , before the supercells relaxation with either  $\text{G}_{\text{SO}}$  or  $\text{C}_{\text{SO}}$   $\text{V}^{3+}$  spin orders. Indirectly, we apply a magnetic field. Remarkably, only the  $\text{C}_{\text{SO}}$ /F-type magnetic configuration yields a significant net magnetic moment along the [110] direction for  $\text{V}^{3+}$  with with  $3.955 \mu_B$  (8 f.u.)<sup>-1</sup> and illustrated in Figure 4(d) (see Table S6 in ref. [40]). Although the  $\text{G}_{\text{SO}}$  is more stable after ZFC, only the forced ferromagnetic alignment of the  $\text{Pr}^{3+}$  with  $\mathbf{B}$  and  $\text{C}_{\text{SO}}$  ordering of the  $\text{V}^{3+}$  spins yield a net magnetization of along the [110] direction, further rationalizing the  $\text{V}^{3+}$  spins reordering. Experimentally, we have only observed an open hysteretic cycle for  $\text{V}^{3+}$  when  $\mathbf{B}$  was along the [110] direction. For  $\text{Pr}^{3+}$ , angle dependent measurements showed that  $\langle L_z \rangle$  is constant at saturation, whereas it vanishes at remanence when  $\mathbf{B}$  is along the [100] or [010] directions (see Figure S4 in ref. [40]). This anisotropic behavior at remanence suggests that the magnetic polarizability of  $\text{Pr}^{3+}$  depends also on crystalline structure. For instance, the off-centering of the  $\text{Pr}^{3+}$  ion from its position in cubic symmetry and/or  $\text{V}^{3+}$   $3d$  orbital ordering (entangled with spin orders) could lead to a change in the orbital sector, tuning  $\langle L_z \rangle$  through perturbation of the single-ion anisotropy.

## F. Strain engineering.

To gain more insight into the coupling mechanisms, we present in Figure 5(a) the first macroscopic magnetization curves as a function of  $V_{\text{UC}}$ , measured with  $\mathbf{B}$  applied along the [110] direction. For small  $V_{\text{UC}}$  (black curve, #1), the magnetization smoothly rises with  $\mathbf{B}$  until the saturation. A kink around 20 kOe corresponds to the metamagnetic transition.

Its curvature increases with  $V_{\text{UC}}$  so that the curve mirrors (blue curve, #4) that of  $\mathcal{A}_{V^{3+}}$  in Figure 4(c), interpreted as the  $V^{3+}$  spin reorientation from  $G_{\text{SO}}$  to  $C_{\text{SO}}$ . In Figure 5(b),  $\mathcal{A}_{V^{3+}}$  (at saturation) and  $\langle L_z \rangle$  (at remanence and saturation) are displayed as a function of  $V_{\text{UC}}$ . Overall the amplitude of  $\langle L_z \rangle$  decreases as  $V_{\text{UC}}$  increases, albeit slightly at saturation, and the non linear dependence and  $\mathcal{A}_{V^{3+}}$  versus  $V_{\text{UC}}$  recalls the dependence of  $T_{\text{SO}}$  in Figure 1(k). Thus, the behaviors of  $\langle L_z \rangle$  and  $\mathcal{A}_{V^{3+}}$  at the microscopic scale agrees the macroscopic measurements in Figure 1. Additionally, normalized XMCD loops for films with small and large  $V_{\text{UC}}$  (see Figure S6 in ref. [40]) are in agreement with hysteretic loops in Figure 1, especially for Pr- $M_{4,5}$  edges. This raises the question of the change of the  $\text{Pr}^{3+}$  cuboctahedral environment, as shown in Figure 1(a), its impact on magnetic properties. In Figure 5(c), we show the XAS spectra recorded at the O-K, varying  $V_{\text{UC}}$  of the films. The observed features correspond to the transition from O  $1s$  to O  $2p$  orbitals, hybridized with the empty orbital states of the V and Pr cations, thereby sensitive to their surrounding environment. The intensity of the peaks increases as  $V_{\text{UC}}$  decreases, consistently with a higher hybridization in small unit cell. The broad peak around 542.5 eV and the peaks around 535 eV correspond to the V  $4sp$  and Pr  $5d$  hybridized orbitals, respectively. The peaks at 529 eV and 531 eV, partially obscured by additional peaks for small  $V_{\text{UC}}$ , correspond to the O  $2p$  overlap with the crystal field split V  $3d t_{2g}$  and  $e_g$  orbitals, respectively. In Figure 5(d), we show, against  $V_{\text{UC}}$ , the energy of the O  $2p$  – Pr  $5d$  hybridized peaks, whose bonding characters, in a quasitrigonal environment, correspond to  $\sigma$ -bonds ( $5d\sigma$ ),  $\pi$ -bonds ( $5d\pi$ ) and Pr  $5d_{z^2}$  bonds ( $5da_1$ ) with O  $2p$  character mixed in [62]. The Pr  $5da_1$  shows a slight shift, and its intensity vanishes as  $V_{\text{UC}}$  increases. The Pr  $5d\pi$  and Pr  $5d\sigma$  peaks shift towards higher and lower energy, respectively. We attribute these shifts to the elongation of the O  $2p$  – Pr  $5d\sigma$  bond and shrinking of the O  $2p$  – Pr  $5d\pi$  bond with increasing  $V_{\text{UC}}$ .

We used DFT calculations to assess the structural changes of  $\text{PrVO}_3$  under strain along the [110] direction and the evolution of the Pr–O bond lengths (see above). The bonds increases (up to 6%) for Pr atoms bound with all apical O atoms of the  $\text{VO}_6$  octahedron, while they decreases (approx.  $-1.5\%$ ) for Pr atoms bound with some equatorial O atoms, especially along the [110] direction (see Figure S7 in ref. [40]). Thus, this suggests that the highly directional  $5d\sigma$  bonds are sensitive to an elongation involving apical oxygen [highlighted in Figure 1(a)] and that the shrinking of the  $5d\pi$  bonds involves oxygen in the equatorial plane of the  $\text{VO}_6$  octahedra. The measured energy shifts hence indirectly

capture the distortion of the  $\text{VO}_6$  octahedra through changes of the cuboctahedral environment of  $\text{Pr}^{3+}$ . Recently, theoretical investigations have highlighted the role played by the Dzyaloshinski-Moriya interactions and magnetostructural couplings involving the oxygen octahedra rotation in the understanding of the polarization of the  $\text{R}^{3+}$  magnetic moment in orthorhombic perovskites [11, 23]. For instance, Zhao *et al.* have considered an energy term as  $\Delta E_{\text{R}^{3+}} \propto -(\omega_- \times \mathbf{G}_{\text{SO}} + \omega_+ \times \mathbf{C}_{\text{SO}}) \cdot \mathbf{F}^{\text{R}^{3+}}$  among the magnetic interactions between the cations [11].  $\mathbf{F}^{\text{R}^{3+}}$  is the net magnetization of  $\text{R}^{3+}$ ,  $\omega$  is a pseudo-vector representing in-phase (+) or out-of-phase (-) octahedral rotations, and  $\mathbf{C}_{\text{SO}}/\mathbf{G}_{\text{SO}}$  is a vector representing the spin order of the transition metal [63]. In the parent compound  $\text{LaVO}_3$ , which is also (110)-oriented when grown on  $\text{SrTiO}_3$ , the  $a^-a^+c^-$  tilt system has been determined experimentally [64]. This indicates that the in-phase rotation axis lies in the substrate plane, as deduced indirectly in  $\text{PrVO}_3$  and  $\text{LaVO}_3$  films by mapping the  $\text{R}^{3+}$  cation displacements [65], which are coupled to the rotations through a trilinear energetic term [66, 67]. Thereby, the  $\text{V}^{3+}$  spin is  $\mathbf{G}_{\text{SO}}$  in our case after ZFC, and  $\omega_-$  and  $\omega_+$  are parallel to the [010] and [001] directions, respectively. From Figure 1(a), we consider the  $\text{V}^{3+}$  spins align along  $c$  for  $\mathbf{G}_{\text{SO}}$  and within the  $ab$  plane for  $\mathbf{C}_{\text{SO}}$  (assuming the  $b$ -component is the strongest as in the bulk material [56]). Consequently, we can write  $\Delta E_{\text{R}^{3+}} \propto -(|\omega_-| \cdot |\mathbf{G}_{\text{SO}}| + |\omega_+| \cdot |\mathbf{C}_{\text{SO}}|) \cdot |\mathbf{F}^{\text{R}^{3+}}|$  along the  $[100]_o$  direction, for simplicity. We observe that depending on the  $\mathbf{F}^{\text{R}^{3+}}$  direction, the first or the second term of  $\Delta E_{\text{R}^{3+}}$  will gain energy, with  $\mathbf{F}^{\text{R}^{3+}}$  along [100] or  $[\bar{1}00]$ , respectively. In turn, it will promote a spin  $\text{V}^{3+}$  reorientation. As  $\mathbf{B}$  contributes to align the  $\text{Pr}^{3+}$  magnetic moments, it will induce a spin reordering from  $\mathbf{G}_{\text{SO}}$  to  $\mathbf{C}_{\text{SO}}$  as in  $\text{DyVO}_3$  [68], and promote a net magnetic moment on the  $\text{V}^{3+}$  sublattice as observed in Figure 4. Hence, tailoring the octahedral site rotations and distortions should allow tuning the  $3d-4f$  exchange interaction and the energy balance between the different ordered states.

### G. Tailoring distortions and exchange couplings.

To gain further insights, we calculated the amplitude of the distortion modes in  $\text{PrVO}_3$  films as a function of the elongation along the [110] direction by DFT (see above and in ref. [40]). Four primary distortions are active: two octahedral rotations  $\varphi_z^+$ ,  $\varphi_{xy}^-$  ( $\varphi_x^- + \varphi_y^-$ ), an antipolar motion of  $\text{R}^{3+}$  cations  $X_5^-$  and a JT mode  $Q_2^+$  [14]. Their amplitude as function of  $V_{\text{UC}}$  is presented in Figure 6(a)-(d), respectively. The [001] axis of in-phase rotation

lies in the substrate plane, resulting in a minimal  $\varphi_z^+$  rotation due to substrate clamping [Figure 6(a)]. In contrast, the [110] axis of the out-of-phase rotation is free, and the  $\varphi_{xy}^-$  rotation increases with  $V_{UC}$  [Figure 6(b)]. This increase is known to favor a  $C_{OO}$  ground state in bulk  $RVO_3$  [21] but it promotes also the anti-polar  $X_5^-$  motion [16, 70] of the  $Pr^{3+}$  ions in the  $ab$  plane [Figure 6(c)]. We note the [110] axis elongation appears then as an appealing means for enhancing the electric polarization driven by hybrid improper ferroelectricity [13–15, 17, 18]. The  $X_5^-$  motion forces the appearance of the  $Q_2^+$  distortion mode [Figure 6(d)], but exhibiting a non-monotonous behavior versus  $V_{UC}$  that is reminiscent of the trends in  $T_{SO}$  and  $\mathcal{A}_{V^{3+}}$  displayed in Figure 1(k) and Figure 5(c), respectively. This indicates that the superexchange interactions between V sites are mainly driven by the  $Q_2^+$  octahedral-site distortion (linked to the octahedral rotation and cation displacements [14]) in our films. Consequently, it promotes a  $C_{OO}$  ground state, associated with  $G_{SO}$ . The strengthening of  $\varphi_{xy}^-$  and  $Q_2^+$  as  $V_{UC}$  increases should stabilize further a  $C_{OO}/G_{SO}$  ground state. However,  $Q_2^+$  is destabilized for large  $V_{UC}$ , suggesting alternative means for energy gain. The decrease of the  $Q_2^+$  distortion may suggest a potential larger energy gain associated to the  $Q_2^-$  Jahn-Teller distortion and its  $G_{OO}$  ordering as shown in bulk perovskite oxides [69–71]. Thus, the response of the system when applying  $\mathbf{B}$ , forcing the  $V^{3+}$  spins alignment in the  $ab$  plane, will be the promotion of  $C_{SO}$ , and concomitantly a  $G_{OO}/Q_2^-$  state to gain energy. We point out this should also favor an alternative antipolar  $X_3^-$  motion of the  $Pr^{3+}$  cations along the  $c$ -axis [14]. The lattice distortions act thus as a tuning knob enabling the competition between  $C_{SO}/G_{OO}$  and  $G_{SO}/C_{OO}$  states, as seen in Figure 5 where  $G_{SO}$  resists until the spins switch to  $C_{SO}$ , as  $V_{UC}$  increases. In turn, octahedral-site JT modifications will also yield changes in the cuboctahedral environment surrounding  $Pr^{3+}$ .

We have seen previously that structural changes due to the lattice expansion affect the hybridization between orbitals [see Fig. 5(c) and (d)]. We now probe these changes when the temperature or  $\mathbf{B}$  are varied. Figure 6(e) and (g) display the O-K edge XAS spectra as a function of the temperature ( $|\mathbf{B}| = 65$  kOe) and the magnetic field  $\mathbf{B}$  at 5 K after ZFC, respectively. Figure 6(f) and (h) show the corresponding energy shifts of the O  $2p - Pr$   $5d\sigma$  and O  $2p - Pr$   $5d\pi$  hybridized peaks relative to 300 K and zero field, respectively. Notably, the energy of the O  $2p - V$   $4sp$  peak, indicated by a dashed line, remains constant at  $542.55 \pm 0.03$  eV, during the temperature or magnetic field variation. The  $5d\sigma$  peak shift towards higher energies in Figure 6(f) bottom panel and indicates that the length



of  $\sigma$ -bonds decreases due to the volume contraction as the temperature decreases. The  $5d\pi$  peak exhibits energy shifts [see Figure 6(f) top panel], indicating an initial  $\pi$ -bonds elongation, a subsequent shrink below 100 K, and a further elongation below 40 K. The shift at 100 K indicates the  $\text{Pr}^{3+}$  magnetic sublattice polarization with the onset of the  $\text{V}^{3+}$  spin ordering around  $T_{\text{SO}}$ , likely reminiscent of magnetostriction. As a reversal of  $\langle L_z \rangle$  at remanence occurs between 5 and 40 K [Figure 3(b)], these shift around 40 K indicates the modifications of octahedral-site distortions, likely reminiscent orbital order switching. Figure 6(h) shows the  $5d\pi$ , at 5 K (after ZFC), initially shifting towards high energy up to 10 kOe, then decreasing and returning back to its initial energy position at remanence. In contrast, the  $5d\sigma$  peak energy drops by  $-0.4$  eV, maintaining this energy position even at remanence. We attribute the change of the O  $2p$  – Pr  $5d$  hybridization to the modifications of the  $\text{VO}_6$  octahedral environment (see ref. [40] for DFT calculations at the collinear level) with the reorientation of the  $\text{V}^{3+}$  spins from  $G_{\text{SO}}$  to  $C_{\text{SO}}$  (rotation of the Néel vector), accompanied by a reversal of  $\langle L_z \rangle$  observed in Figure 4. However, the behavior of the shift of the Pr  $5d$  peak's energy is not entirely reversible with  $\mathbf{B}$  and it suggests a pinning to atomic disorder or the mutual polarization between the  $\text{Pr}^{3+}$  and  $\text{V}^{3+}$  magnetic sublattices. Consequently, an exchange strictive structural bias may foster the coexistence of multiple states [21, 68] and/or contribute to the observed large coercive fields as structural distortion,  $\text{V}^{3+}$  spin reorientation and  $\text{Pr}^{3+}$  magnetic moments are interlocked. Finally in the case of coexisting orbital orders,  $Q_2^+$  and  $Q_2^-$  JT distortions would be active simultaneously, both coupled to  $X_3^-$  [14]. The resulting trilinear coupling has been identified as a key structural mode for controlling spins with an electric polarization in designed superlattices, paving the way towards orthorhombic perovskite based magnetoelectric multiferroics [14].

#### IV. CONCLUSION

In conclusion, we have shown that magnetization reversal and spin reorientation in  $\text{PrVO}_3$  thin films involve the coupling between the antiferromagnetic  $\text{V}^{3+}$  and paramagnetic  $\text{Pr}^{3+}$  sublattices, with the canted  $3d$  spins and  $4f$  moments compensating each other as a function of the temperature. Through uniaxial strain engineering, we evidenced that the lattice distortions act on the exchange interaction between  $\text{V}^{3+}$  and  $\text{Pr}^{3+}$  cations, and consequently have a strong influence on the  $\text{V}^{3+}$  spin and orbital orderings, assisted by a change of the

cooperative Jahn-Teller distortion mode. Associated to the rare earth atomic displacements  $X_5^-$  and  $X_3^-$  in perovskite oxides, the consideration of these key magnetostructural coupling between A and B cations opens up new insights for the design of robust magnetoelectric multiferroics. The nature of the A-site atom, its single-ion anisotropy and spin-orbit coupling should also be considered systematically for the understanding of the complexity in TMO.

## ACKNOWLEDGMENTS

OC thanks B. Raveau and M. Seikh for stimulating discussions. This work was supported by the French National Research Agency (ANR) under project CITRON (ANR-21-CE09-0032), the Région Grand Est under project RHUM (AAP-013-075), and the France 2030 government investment plan under grant PEPR SPIN - SPINMAT (ANR-22-EXSP-0007). The work has benefited of the resources of experimental platforms at IJL: Tube Davm (funded by FEDER EU, ANR, Région Grand Est, and Métropole Grand Nancy), Magnetism & Cryogenics, and XGamma, all supported by the LUE-N4S project, part of the French PIA project Lorraine Université d'Excellence (ANR-15IDEX-04-LUE), and by FEDER-FSE Lorraine et Massif Vosges 2014-2020, an EU program. The XAS experiments were performed on the DEIMOS beamline at SOLEIL Synchrotron (proposal number 20130636). We are grateful to the SOLEIL staff for smoothly running the facility. The first-principles calculations were conducted on the Abel supercomputers (PRACE project TheoMoMuLaM), the Cartesius supercomputer (PRACE project TheDeNoMO), and the Tier-1 supercomputer of the Fédération Wallonie-Bruxelles, funded by the Walloon Region (Grant No 1117545). Additional resources were provided by the Céci-HPC facilities, funded by F.R.S.-FNRS (Grant No 2.5020.1). JV acknowledges access granted to High Performance Computing resources of CRIANN through the projects 2020005 and 2007013 and of CINES through the DARI project A0080911453.

- 
- [1] J. Goodenough, Electronic and ionic transport properties and other physical aspects of perovskites, *Rep. Prog. Phys.* **67**, 1915 (2004).
  - [2] M. Imada, A. Fujimori, and Y. Tokura, Metal-insulator transitions, *Rev. Mod. Phys.* **70**, 1039 (1998).

- [3] Y. Tokura and N. Nagaosa, Orbital physics in transition-metal oxides, *Science* **288**, 462 (2000).
- [4] P. Zubko, S. Gariglio, M. Gabay, P. Ghosez, and J.-M. Triscone, Interface physics in complex oxide heterostructures, *Annu. Rev. Condens. Matter Phys.* **2**, 141 (2011).
- [5] M. Coll, J. Fontcuberta, M. Althammer, M. Bibes, H. Boschker, A. Calleja, G. Cheng, M. Cuoco, R. Dittmann, B. Dkhil, I. E. Baggari, M. Fanciulli, E. F. I. Fina, C. Frontera, S. Fujita, V. Garcia, S. T. B. Goennenwein, C. G. Granqvist, J. Grollier, *et al.*, Towards oxide electronics: A roadmap, *Appl. Surf. Sci.* **482**, 1 (2019).
- [6] E. Bousquet and A. Cano, Non-collinear magnetism in multiferroic perovskites, *J. Phys.: Condens. Matter* **28**, 123001 (2016).
- [7] A. Fert, R. Ramesh, V. Garcia, F. Casanova, and M. Bibes, Electrical control of magnetism by electric field and current-induced torques, *Rev. Mod. Phys.* **96**, 015005 (2024).
- [8] Y. Tokura and S. Seki, Multiferroics with spiral spin orders, *Adv. Mater.* **22**, 1554 (2010).
- [9] T. Kimura, T. Goto, H. Shintani, K. Ishizaka, T. Arima, and Y. Tokura, Magnetic control of ferroelectric polarization, *Nature* **426**, 55 (2003).
- [10] S. Manipatruni, D. E. Nikonov, C.-C. Lin, T. Gosavi, H. Liu, B. Prasad, Y.-L. Huang, E. Bonturim, R. Ramesh, and I. A. Young, Scalable energy-efficient magnetoelectric spin-orbit logic, *Nature* **565**, 35 (2019).
- [11] H. J. Zhao, J. Íñiguez, X. Chen, and L. Bellaiche, Origin of the magnetization and compensation temperature in rare-earth orthoferrites and orthochromates, *Phys. Rev. B* **93**, 014417 (2016).
- [12] H. J. Zhao, L. Bellaiche, X. M. Chen, and J. Íñiguez, Improper electric polarization in simple perovskite oxides with two magnetic sublattices, *Nat. Commun.* **8**, 14025 (2016).
- [13] J. M. Rondinelli and C. J. Fennie, Octahedral rotation-induced ferroelectricity in cation ordered perovskites, *Adv. Mater.* **24**, 1961 (2012).
- [14] J. Varignon, N. C. Bristowe, E. Bousquet, and P. Ghosez, Coupling and electrical control of structural, orbital and magnetic orders in perovskites, *Sci. Rep.* **5**, 15364 (2015).
- [15] N. A. Spaldin and R. Ramesh, Advances in magnetoelectric multiferroics, *Nat. Mater.* **18**, 203 (2007).
- [16] J. B. Goodenough, Metallic oxides, *Prog. Solid State Chem.* **5**, 145 (1971).
- [17] E. Bousquet, N. Stucki, C. Lichtensteiger, P. Hermet, S. Gariglio, J.-M. Triscone, and P. Ghosez, Improper ferroelectricity in perovskite oxide artificial superlattices, *Nature* **452**, 732

- (2008).
- [18] N. A. Benedek and C. J. Fennie, Hybrid improper ferroelectricity: A mechanism for controllable polarization-magnetization coupling, *Phys. Rev. Lett.* **106**, 107204 (2011).
  - [19] S. Miyasaka, Y. Okimoto, M. Iwama, and Y. Tokura, Spin-orbital phase diagram of perovskite type  $RVO_3$  ( $R$  = rare-earth ion or Y), *Phys. Rev. B* **68**, 100406(R) (2003).
  - [20] E. Dagotto, Complexity in strongly correlated electronic systems, *Science* **309**, 257 (2005).
  - [21] M. H. Sage, G. R. Blake, C. Marquina, and T. T. M. Palstra, Competing orbital ordering in  $RVO_3$  compounds: High-resolution x-ray diffraction and thermal expansion, *Phys. Rev. B* **76**, 195102 (2007).
  - [22] P. Radhakrishnan, K. S. Rabinovich, A. V. Boris, K. Fürsich, M. Minola, G. Christiani, G. Logvenov, B. Keimer, and E. Benckiser, Imprinted atomic displacements drive spin-orbital order in a vanadate perovskite, *Nat. Phys.*, <https://doi.org/10.1038/s41567-024-02686-8> (2024).
  - [23] A. Sasani, J. Íñiguez, and E. Bousquet, Magnetic phase diagram of rare-earth orthorhombic perovskite oxides, *Phys. Rev. B* **104**, 064431 (2021).
  - [24] D. Li, K. Lee, B. Y. Wang, M. Osada, S. Crossley, H. R. Lee, Y. Cui, Y. Hikita, and H. Y. Hwang, Superconductivity in an infinite-layer nickelate, *Nature* **572**, 624 (2019).
  - [25] B. Y. W. T. C. Wang, Y. T. Hsu, M. Osada, K. Lee, C. Jia, C. Duffy, D. Li, J. Fowlie, M. R. Beasley, T. P. Devereaux, I. R. Fisher, N. E. Hussey, and H. Y. Hwang, Effects of rare-earth magnetism on the superconducting upper critical field in infinite-layer nickelates, *Sci. Adv.* **9**, eadf6655 (2023).
  - [26] J.-S. Zhou and J. B. Goodenough, Intrinsic structural distortion in orthorhombic perovskite oxides, *Phys. Rev. B* **77**, 132104 (2008).
  - [27] A. M. Glazer, The classification of tilted octahedra in perovskites, *Acta Crystallogr.* **B28**, 3384 (1972).
  - [28] J.-S. Zhou and J. B. Goodenough, Universal octahedral-site distortion in orthorhombic perovskite oxides, *Phys. Rev. Lett.* **94**, 065501 (2005).
  - [29] J.-S. Zhou, J. A. Alonso, V. Pomjakushin, J. B. Goodenough, Y. Ren, J.-Q. Yan, and J.-G. Cheng, Intrinsic structural distortion and superexchange interaction in the orthorhombic rare-earth perovskites  $RCrO_3$ , *Phys. Rev. B* **81**, 214115 (2010).
  - [30] P. Ohresser, E. Otero, F. Choueikani, K. Chen, S. Stanescu, F. Deschamps, T. Moreno, F. Polack, B. Lagarde, J.-P. Daguerre, F. Marteau, F. Scheurer, L. Joly, J.-P. Kappler, B. Muller,

- O. Bunau, and P. Sainctavit, Deimos: A beamline dedicated to dichroism measurements in the 350–2500 eV energy range, *Rev. Sci. Instrum.* **85**, 013106 (2014).
- [31] B. Thole, P. Carra, F. Sette, and G. van der Laan, X-ray circular dichroism as a probe of orbital magnetization, *Phys. Rev. Lett.* **68**, 1943 (1992).
- [32] P. Carra, B. T. Thole, M. Altarelli, and X. Wang, X-ray circular dichroism and local magnetic fields, *Phys. Rev. Lett.* **70**, 694 (1993).
- [33] G. Kresse and J. Haffner, Ab initio molecular dynamics for liquid metals, *Phys. Rev. B* **47**, 558 (1993).
- [34] G. Kresse and J. Furthmüller, Efficiency of ab-initio total energy calculations for metals and semiconductors using a plane-wave basis set, *Comput. Mater. Sci.* **6**, 15 (1996).
- [35] J. P. Perdew, A. Ruzsinszky, G. I. Csonka, O. A. Vydrov, G. E. Scuseria, L. A. Constantin, X. Zhou, and K. Burke, Restoring the density-gradient expansion for exchange in solids and surfaces, *Phys. Rev. Lett.* **100**, 136406 (2008).
- [36] A. Liechtenstein, V. I. Anisimov, and J. Zaanen, Density-functional theory and strong interactions: Orbital ordering in mott-hubbard insulators, *Phys. Rev. B* **52**, R5467 (1995).
- [37] O. Copie, H. Rotella, P. Boullay, M. Morales, A. Pautrat, P.-E. Janolin, I. C. Infante, D. Pravathana, U. Lüders, and W. Prellier, Structure and magnetism of epitaxial PrVO<sub>3</sub> films, *J. Phys.: Condens. Matter* **25**, 492201 (2013).
- [38] D. Kumar, A. David, A. Fouchet, A. Pautrat, J. Varignon, C. U. Jung, U. Lüders, B. Domengès, O. Copie, P. Ghosez, and W. Prellier, Magnetism tailored by mechanical strain engineering in PrVO<sub>3</sub> thin films, *Phys. Rev. B* **99**, 224405 (2019).
- [39] O. Copie, J. V. H. Rotella, G. Steciuk, P. Boullay, A. Pautrat, A. David, B. Mercey, P. Ghosez, and W. Prellier, Chemical strain engineering of magnetism in oxide thin films, *Adv. Mater.* **29**, 1604112 (2017).
- [40] See Supplemental Material, which includes Refs. [41–50], for XRD measurements of PrVO<sub>3</sub> films grown at different temperatures. Strain and volume versus growth temperature. XRD measurements at low temperatures. Raw V-L<sub>2,3</sub> edges XAS spectra and raw Pr-M<sub>4,5</sub> edges spectra. V-L<sub>2,3</sub> edges and Pr-M<sub>4,5</sub> edges spectra as a function of the polarized light incidence angle. V-L<sub>2,3</sub> edges XMCD and corresponding integrated signal. XMCD hysteretic loops measured at Pr-M<sub>4</sub> edge for film with large and small volume. Schematics of the calculated structure of PrVO<sub>3</sub>. Amplitude (in Å) of the main lattice distortions calculated by DFT considering

- collinear and non-collinear magnetism. Calculated magnetization (in  $\mu_B$ ) at  $V^{3+}$  and  $Pr^{3+}$  site for magnetic configurations.
- [41] Y. Ren, A. A. Nugroho, A. A. Menovsky, J. Stremper and U. Rütt, F. Iga, T. Takabatake, and C. W. Kimball, Orbital-ordering-induced phase transition in  $LaVO_3$  and  $CeVO_3$ , *Phys. Rev. B* **67**, 014107 (2003).
- [42] P.-E. Janolin, Strain on ferroelectric thin films, *J. Mater. Sci* **44**, 5025 (2009).
- [43] A. Vailionis, H. Boschker, W. Siemons, E. P. Houwman, D. H. A. Blank, G. Rijnders, and G. Koster, Misfit strain accommodation in epitaxial  $ABO_3$  perovskites: lattice rotations and lattice modulations, *Phys. Rev. B* **83**, 064101 (2011).
- [44] H. Meley, Karandeep, L. Oberson, J. de Bruijkere, D. T. L. Alexander, J.-M. Triscone, Ph. Ghosez, S. Gariglio, Structural analysis of  $LaVO_3$  thin films under epitaxial strain, *APL Mater.* **6**, 046102 (2018).
- [45] H. Wadati, D. G. Hawthorn, J. Geck, T. Z. Regier, R. I. R. Blyth, T. Higuchi, Y. Hotta, Y. Hikita, H. Y. Hwang, and G. A. Sawatzky, Interface reconstruction in V-oxide heterostructures determined by x-ray absorption spectroscopy, *Appl. Phys. Lett.* **95**, 023115 (2009).
- [46] D. Kumar, A. Fouchet, A. David, A. Cheikh, T. S. Suraj, O. Copie, C. U. Jung, A. Pautrat, M. S. R. Rao, and W. Prellier, Enhancement of magnetic properties in compressively strained  $PrVO_3$  thin films, *Phys. Rev. Materials* **3**, 124413 (2019).
- [47] J. Goedkoop, B. T. Thole, G. van der Laan, G. A. Sawatzky, F. M. F. de Groot, and J. C. Fuggle, Calculations of magnetic x-ray dichroism in the  $3d$  absorption spectra of rare-earth compounds, *Phys. Rev. B* **4**, 2086 (1988).
- [48] V. V. Mehta, S. Bose, J. M. Iwata-Harms, E. Arenholz, C. Leighton, and Y. Suzuki, Ferromagnetism in  $PrCoO_3$  epitaxial films, *Phys. Rev. B* **87**, 020405(R) (2013).
- [49] D. Orobengoa, C. Capillas, M. I. Aroyo, and J. M. Perez-Mato, AMPLIMODES: symmetry-mode analysis on the Bilbao Crystallographic Serve, *J. Appl. Crystallogr.* **42**, 820 (2009).
- [50] J. M. Perez-Mato, D. Orobengoa, and M. I. Aroyo, Mode crystallography of distorted structures, *Acta Crystallogr.* **A66**, 558 (2010).
- [51] Y. Ren, T. T. M. Palstra, D. I. Khomskii, E. Pellegrin, A. A. Nugroho, A. A. Menovsky, and G. A. Sawatzky, Temperature-induced magnetization reversal in a  $YVO_3$  single crystal, *Nature* **396**, 441 (1998).

- [52] Y. Kimishima, Y. Ichiyanagi, K. Shimizu, and T. Mizuno, N-type ferrimagnetism of  $\text{SmVO}_3$ , *J. Magn. Magn. Mater.* **210**, 244 (2000).
- [53] Y. Kimishima, M. Uehara, and T. Saitoh, Ca-doping effects on n-type ferrimagnetism of  $\text{NdVO}_3$ , *Solid State Commun.* **133**, 559 (2005).
- [54] M. Reehuis, C. Ulrich, P. Pattison, B. Ouladdiaf, M. C. Rheinstädter, M. Ohl, L. P. Regnault, M. Miyasaka, Y. Tokura, and B. Keimer, Neutron diffraction study of  $\text{YVO}_3$ ,  $\text{NdVO}_3$ , and  $\text{TbVO}_3$ , *Phys. Rev. B* **73**, 094440 (2006).
- [55] M. Reehuis, C. Ulrich, K. Prokeš, S. Mat’áš, J. Fujioka, S. Miyasaka, Y. Tokura, and B. Keimer, Structural and magnetic phase transitions of the orthovanadates  $\text{RVO}_3$  ( $\text{R} = \text{Dy}, \text{Ho}, \text{Er}$ ) as seen via neutron diffraction, *Phys. Rev. B* **83**, 064404 (2011).
- [56] M. Reehuis, C. Ulrich, P. M. Abdala, P. Pattison, G. Khaliullin, J. Fujioka, S. Miyasaka, Y. Tokura, and B. Keimer, Spin and orbital disordering by hole doping in  $\text{Pr}_{1-x}\text{Ca}_x\text{VO}_3$ , *Phys. Rev. B* **94**, 104436 (2016).
- [57] Y. Cao, P. Shafer, X. Liu, D. Meyers, M. Kareev, S. Middey, J. W. Freeland, E. Arenholz, and J. Chakhalian, Magnetism and electronic structure of  $\text{YTiO}_3$  thin films, *Appl. Phys. Lett.* **107**, 112401 (2015).
- [58] R. Aeschlimann, D. Preziosi, P. Scheiderer, M. Sing, S. Valencia, J. Santamaria, C. Luo, H. Ryll, F. Radu, R. Claessen, C. Piamonteze, and M. Bibes, A living-dead magnetic layer at the surface of ferrimagnetic  $\text{DyTiO}_3$  thin films, *Adv. Mater.* **30**, 1707489 (2018).
- [59] J. Schillé, F. Bertran, M. Finazzi, C. Brouder, J. P. Kappler, and G. Krill,  $4f$  orbital and spin magnetism in cerium intermetallic compounds studied by magnetic circular x-ray dichroism, *Phys. Rev. B* **50**, 2985 (1994).
- [60] Y. Teramura, A. Tanaka, B. T. Thole, and T. Jo, Effect of coulomb interaction on the x-ray magnetic circular dichroism spin sum rule in rare earths, *J. Phys. Soc. Jpn.* **65**, 3056 (1996).
- [61] J. Stöhr, Exploring the microscopic origin of magnetic anisotropies with x-ray magnetic circular dichroism (xmcd) spectroscopy, *J. Magn. Magn. Mater.* **200**, 470 (1999).
- [62] S. Cao, X. Zhang, T. R. Paudel, K. Sinha, X. Wang, X. Jiang, W. Wang, S. Brutsche, J. Wang, P. J. Ryan, J.-W. Kim, X. Cheng, E. Y. Tsymbal, P. A. Dowben, and X. Xu, On the structural origin of the single-ion magnetic anisotropy in  $\text{LuFeO}_3$ , *J. Phys.: Condens. Matter* **28**, 156001 (2016).

- [63] L. Bellaiche, Z. Gui, and I. A. Kornev, A simple law governing coupled magnetic orders in perovskites, *J. Phys.: Condens. Matter* **24**, 312201 (2012).
- [64] H. Rotella, U. Lüders, P.-E. Janolin, V. H. Dao, D. Chateigner, R. Feyerherm, E. Dudzik, and W. Prellier, Octahedral tilting in strained  $\text{LaVO}_3$  thin films, *Phys. Rev. B* **85**, 184101 (2012).
- [65] G. Masset, O. Copie, J. Ghanbaja, K. Dumesnil, L. Pasquier, D. Pierre, and S. Andrieu, Epitaxial growth and structure of  $\text{LaVO}_3$  and  $\text{PrVO}_3$  thin films, *Phys. Rev. Materials* **4**, 064417 (2020).
- [66] S. Amisi, E. Bousquet, K. Katcho, and Ph. Ghosez, First-principles study of structural and vibrational properties of  $\text{SrZrO}_3$ , *Phys. Rev. B* **85**, 064112 (2012).
- [67] N. Miao, N. C. Bristowe, B. Xu, M. J. Verstraete, Ph. Ghosez, First-principles study of the lattice dynamical properties of strontium ruthenate. *J. Phys.: Condens. Matter* **26**, 035401 (2013).
- [68] J. Fujioka, T. Yasue, S. Miyasaka, Y. Yamasaki, T. Arima, H. Sagayama, T. Inami, K. Ishii, and Y. Tokura, Critical competition between two distinct orbital-spin ordered states in perovskite vanadates, *Phys. Rev. B* **82**, 144425 (2010).
- [69] J.-S. Zhou and J. Goodenough, Unusual evolution of the magnetic interactions versus structural distortions in  $\text{RMnO}_3$  perovskites, *Phys. Rev. Lett.* **96**, 247202 (2006).
- [70] T. Mizokawa, D. I. Khomskii, and G. A. Sawatzky, Interplay between orbital ordering and lattice distortions in  $\text{LaMnO}_3$ ,  $\text{YVO}_3$ , and  $\text{YTiO}_3$ , *Phys. Rev. B* **60**, 7309 (1999).
- [71] J. Varignon, M. Bibes, and A. Zunger, Origins versus fingerprints of the Jahn-Teller effect in  $d$ -electron  $\text{ABX}_3$  perovskites, *Phys. Rev. Research* **1**, 033131 (2019).



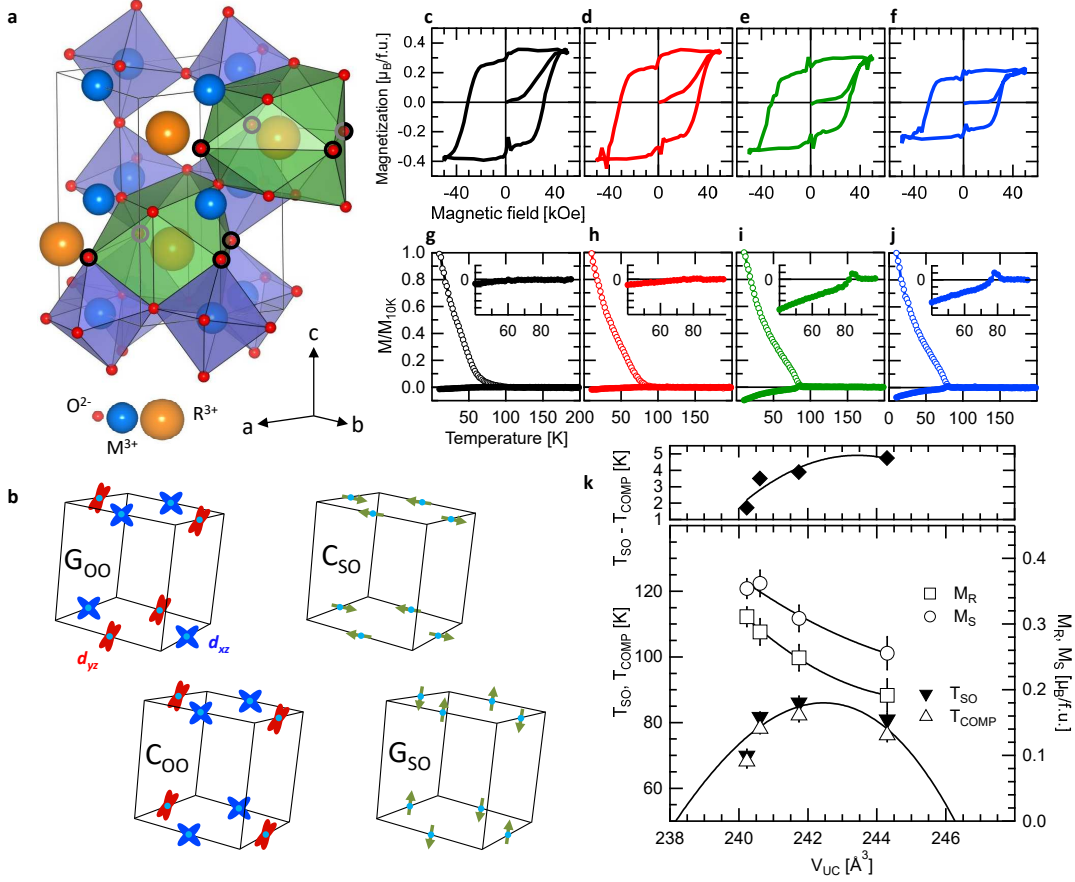


FIG. 1. **Structure, orbital/spin orders of  $RVO_3$ , and  $PrVO_3$  magnetic properties.** (a) Schematic of the orthorhombic structure of  $RVO_3$ .  $V^{3+}$  and  $R^{3+}$  ions are surrounded by 6 oxygen ions (octahedral cage in blue) and the  $R^{3+}$  by 12 oxygen ions (cuboctahedral cage in green), respectively. Some octahedra and cuboctahedra are removed for clarity. (b) Schematics of the orderings of the  $V^{3+}$   $3d_{xz}$  (blue) and  $3d_{yz}$  (red) orbitals and the corresponding spin orderings (the  $3d_{xy}$  orbital is not shown for clarity). Ordering with alternating occupied orbitals in all directions is labelled as  $G_{OO}$ , while the one with identical occupation between consecutive planes along the  $c$ -axis, is labelled as  $C_{OO}$ . The antiferromagnetic  $C_{SO}$  and  $G_{SO}$  spin orders are characterized by spins direction lying in the  $ab$  plane and along the  $c$ -axis, respectively. (c)-(f) At 10 K, magnetization as a function of magnetic field applied parallel to the film's surface, for the films #1, #2, #3 and #4 grown at 800°C (c), 700°C (d), 600°C (e) and 500°C (f), respectively. (g)-(j) Respective normalized magnetization versus temperature after ZFC (full circles) and FC (empty circles). Insets: close-up of the ZFC curves around  $T_{SO}$ . (k) Bottom panel,  $T_{SO}$  and  $T_{COMP}$  temperatures (left axis), and  $M_R$  and  $M_S$  magnetizations (right axis) as function of  $V_{UC}$ . Top panel, difference of  $T_{SO}$  and  $T_{COMP}$ . Lines are guides for the eyes.

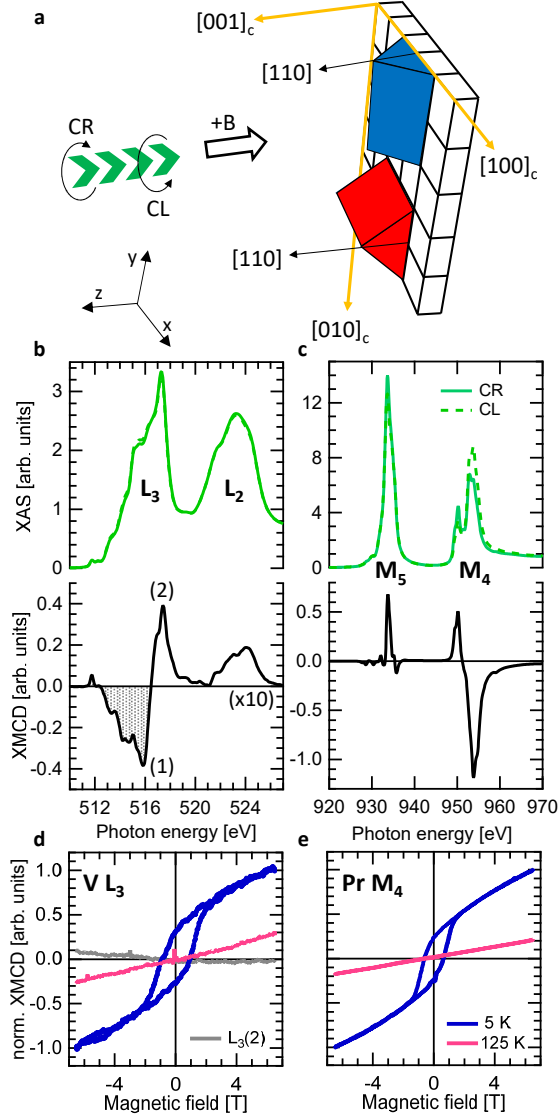


FIG. 2. **XAS and XMCD at low temperatures.** (a) Schematic of the experimental geometry. The incident circularly polarized light, the magnetic field  $\mathbf{B}$ , and the  $[110]$  directions are parallel. (b) V-L<sub>2,3</sub> edges and (c) Pr-M<sub>4,5</sub> edges XAS and XMCD spectra, recorded at  $T = 5$  K with  $|\mathbf{B}| = 65$  kOe. (1) and (2) indicate the position of V-L<sub>3</sub><sup>(1)</sup> (516 eV) and V-L<sub>3</sub><sup>(2)</sup> (517.5 eV), respectively. (d) and (e) XMCD hysteresis loops measured, at 5 K and 125 K, at V-L<sub>3</sub><sup>(1)(2)</sup> edges and XMCD Pr-M<sub>4</sub>, respectively.

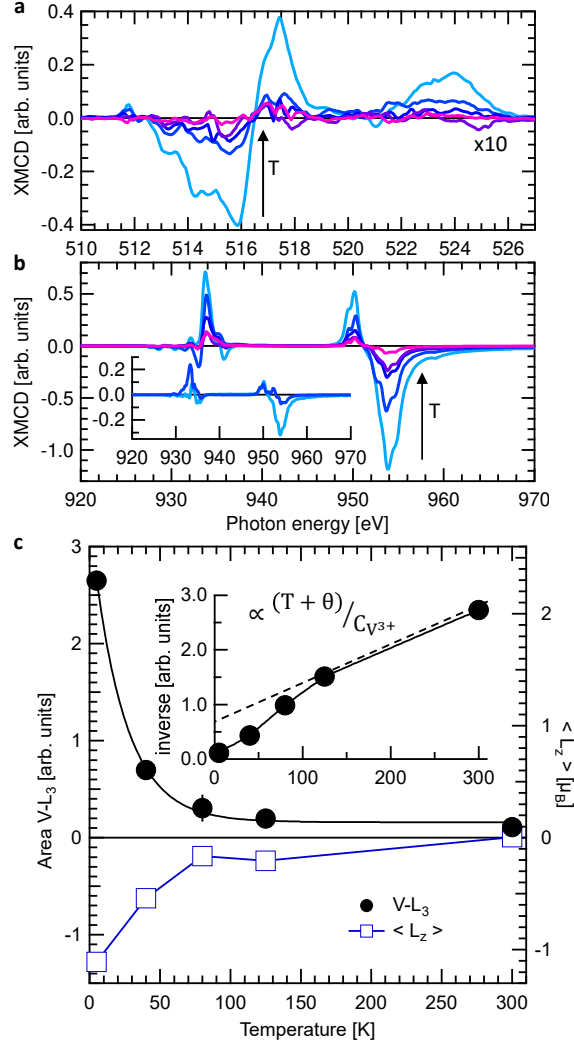


FIG. 3. XMCD spectra as a function of the temperature. (a) V-L<sub>2,3</sub> edges and (b) Pr-M<sub>4,5</sub> edges XMCD spectra recorded at 5 K, 40 K, 80 K, 125 K and 300 K (light blue to violet lines) with  $|\mathbf{B}| = 65$  kOe. The inset of (b) displays the remanent dichroic signal of recorded at 5 K and 40 K. (c) V-L<sub>3</sub> area and Pr-M<sub>4</sub> intensity versus temperature (lines are guide for the eyes). The inset displays the inverse of V-L<sub>3</sub>. The black dashed line is guide for the eyes.

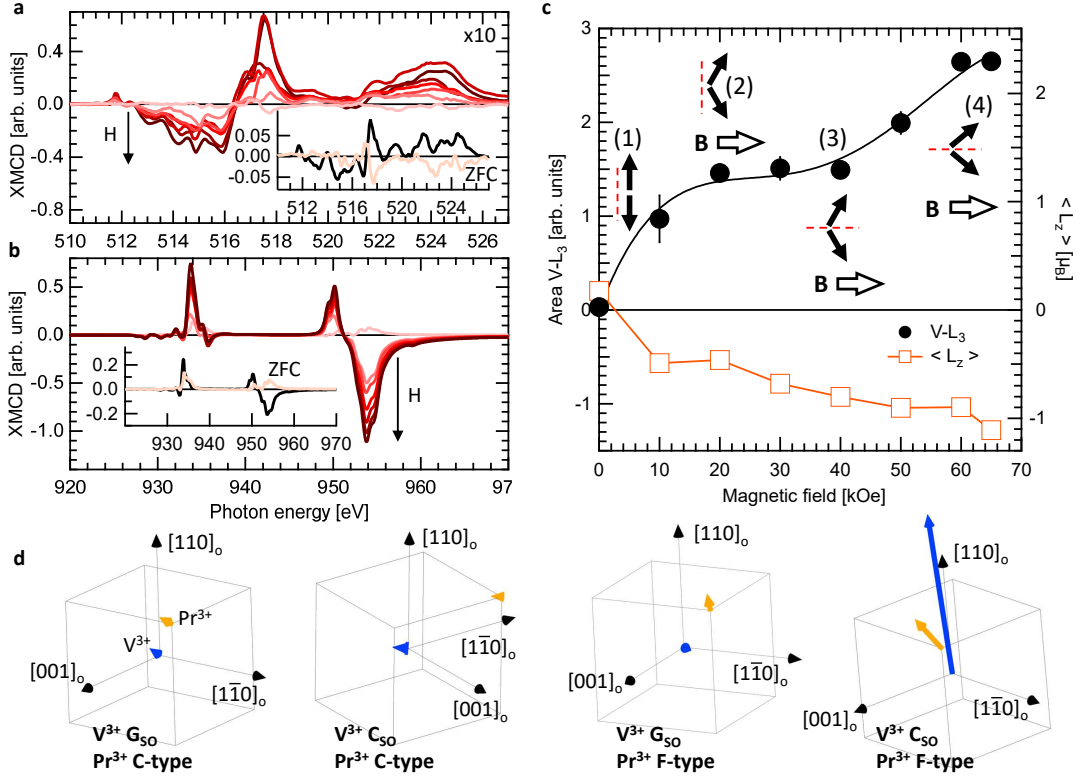


FIG. 4. XMCD as a function of  $B$ , at 5 K after ZFC. (a) V-L<sub>2,3</sub> edges and (b) Pr-M<sub>4,5</sub> edges XMCD spectra.  $|B|$  is varied from 0 Oe to 60 kOe (10 kOe step) up to 65 kOe (light brown to dark brown lines). The insets display the comparison between remanent (black) and ZFC (light brown) dichroic signal at V-L<sub>2,3</sub> edges (a) and Pr-M<sub>4,5</sub> edges (b). (c) V-L<sub>3</sub> area and  $\langle L_z \rangle$  versus  $B$  (lines are guide for the eyes). (d) sketches of the calculated magnetic configurations of V<sup>3+</sup> and Pr<sup>3+</sup>. In the right magnetic configuration, the blue vector's magnitude is divided by 3.

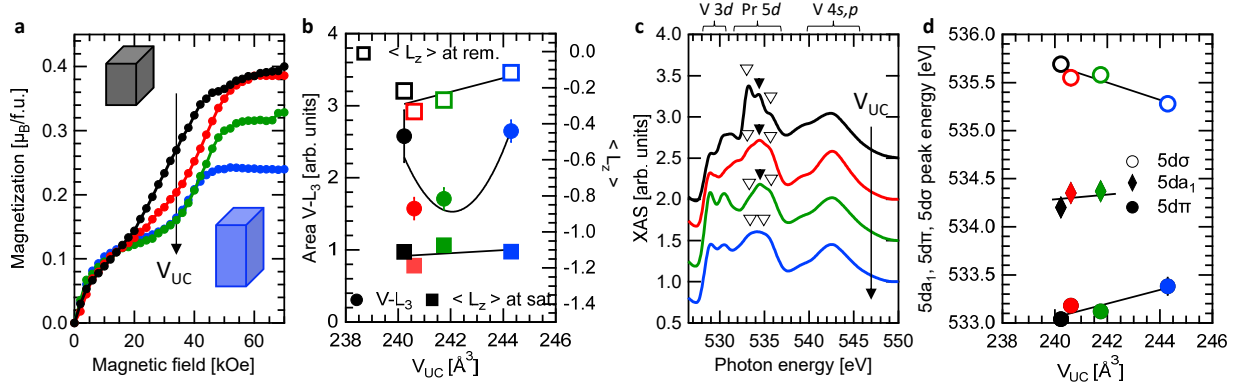


FIG. 5. **Magnetic properties versus  $V_{UC}$ , at 5 K.** (a) Macroscopic first magnetization curves measured for films (#1 to #4) with different  $V_{UC}$ , with  $\mathbf{B}$  perpendicular to the film's surface. (b) and V-L<sub>3</sub> area (at saturation) and  $\langle L_z \rangle$  (square), at remanence (open symbol) and at saturation (closed symbol), versus  $V_{UC}$ . (c) O-K edge XAS spectra for films with different  $V_{UC}$ . The peak energy of the V (3d and 4sp) and Pr (5d) orbitals hybridized with the O 2p orbitals are indicated. (d) Peak energy of the Pr 5d hybridized orbitals (5d<sub>σ</sub>, 5d<sub>a<sub>1</sub></sub>, 5d<sub>π</sub>) as a function of  $V_{UC}$ . The line is guide for the eyes.

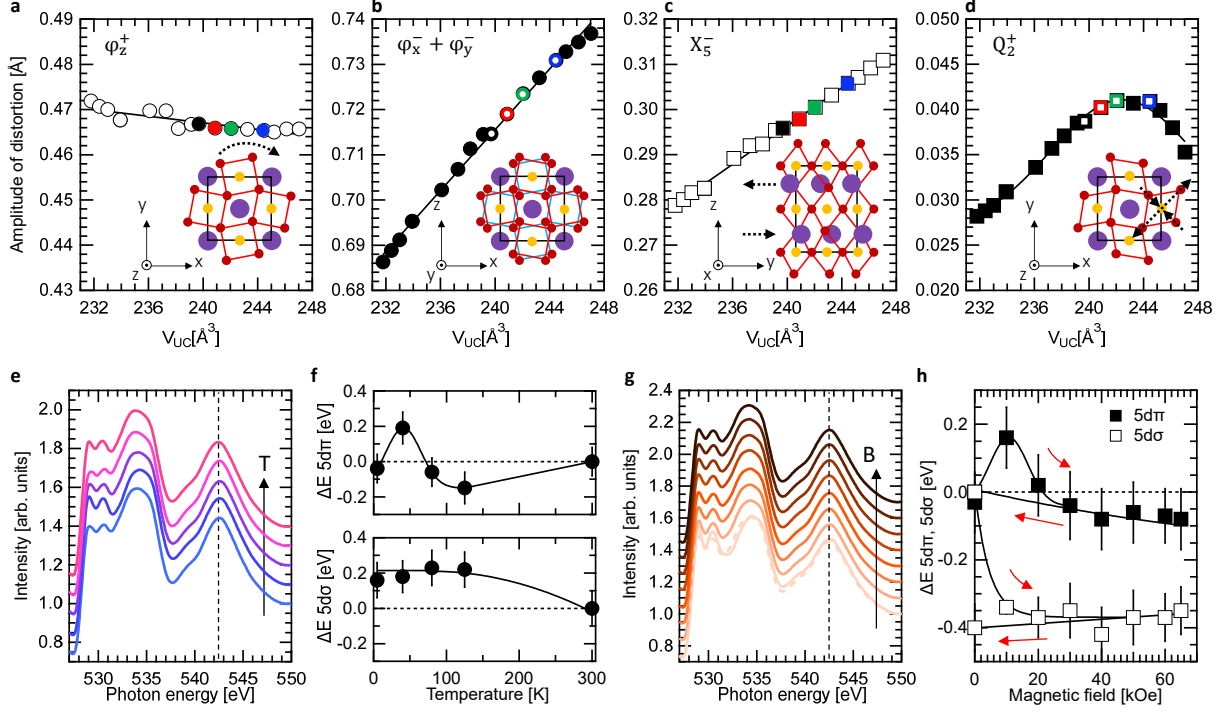


FIG. 6. **Lattice distortions and O 2p – Pr 5d orbitals hybridization.** (a)-(d)  $\varphi_z^+$ ,  $\varphi_{xy}^-$  ( $\varphi_x^- + \varphi_y^-$ ),  $X_5^-$  and  $Q_2^+$  calculated lattice distortions versus  $V_{UC}$ , respectively. The calculated data corresponding to the deposited films (#1 to #4) are marked with colored symbol. (e) O-K edge XAS spectra versus temperature, with  $|\mathbf{B}| = 65$  kOe. (f) Peak energy shift (with respect to the spectrum at 300 K) of the Pr  $5d\sigma$  and  $5d\pi$  hybridized orbitals versus temperature, with  $|\mathbf{B}| = 65$  kOe. (g) At 5 K and after ZFC, O-K edge XAS spectra versus  $\mathbf{B}$ .  $|\mathbf{B}|$  is varied from 0 Oe to 60 kOe (10 kOe step) up to 65 kOe (light brown to dark brown lines). The measurement at remanence is show in dashed light brown line. (h) Peak energy shift (with respect to the spectrum after ZFC) of the Pr  $5d\sigma$  and  $5d\pi$  hybridized orbitals versus  $\mathbf{B}$ . The line is guide for the eyes.